ZEOLITE SYNTHESIS

A priori control of zeolite phase competition and intergrowth with high-throughput simulations

Daniel Schwalbe-Koda[1], Soonhyoung Kwon[2], Cecilia Paris[3], Estefania Bello-Jurado[3], Zach Jensen[1], Elsa Olivetti[1], Tom Willhammar[4], Avelino Corma[3], Yuriy Román-Leshkov[2], Manuel Moliner[3]*, Rafael Gómez-Bombarelli[1]*

Zeolites are versatile catalysts and molecular sieves with large topological diversity, but managing phase competition in zeolite synthesis is an empirical, labor-intensive task. In this work, we controlled phase selectivity in templated zeolite synthesis from first principles by combining high-throughput atomistic simulations, literature mining, human-computer interaction, synthesis, and characterization. Proposed binding metrics distilled from more than 586,000 zeolite-molecule simulations reproduced the extracted literature and rationalized framework competition in the design of organic structure-directing agents. Energetic, geometric, and electrostatic descriptors of template molecules were found to regulate synthetic accessibility windows and aluminum distributions in pure-phase zeolites. Furthermore, these parameters allowed us to realize an intergrowth zeolite through a single bi-selective template. The computation-first approach enables control of both zeolite synthesis and structure composition using a priori theoretical descriptors.

Zeolites are nanoporous materials with a wide range of applications in industrial and sustainable catalysis and separations (*1*, *2*). Although topological diversity makes zeolites versatile, this diversity stems from phase competition between metastable polymorphs, which hinders the rational design of new synthesis routes for zeolites (*3*–*5*). Computer simulations can guide experimental work by predicting the affinity between organic structure-directing agents (OSDAs) and targeted topologies (*6*–*8*). Recent studies have adopted this strategy by simulating up to thousands of OSDAs for a few frameworks at a time (*8*–*10*), but they have been unable to predict whether the proposed OSDAs are more favorable toward another zeolite rather than the desired ones. Accordingly, relatively few experimental realizations have been reported from such studies, because computer-designed OSDA candidates often fail to crystallize the targeted structures. Additionally, design algorithms usually lead to molecules with low synthetic accessibility (*6*, *11*). Manual literature analysis can inform heuristics for zeolite synthesis and avoid expensive simulations (*12*), but datasets compiled from tens of papers are limited in their ability to explain phase selectivity in combinatorial host-guest pairings and have only been attempted for template-free synthesis routes. Finally, although several databases of experimental and hypothetical zeolite structures exist (*13*–*15*), few datasets containing OSDAs or OSDA-zeolite affinities are publicly available. A general approach to simultaneously rationalize phase competition of zeolites, retroactively validate synthesis routes from the literature, control the trade-off between OSDA selectivity and synthetic complexity, and tailor the heteroatom distribution of the targeted materials has not yet been realized. In this work, we simulated over half a million zeolite-OSDA pairs, proposed design principles that outperformed traditional binding energy metrics in reproducing synthesis outcomes from more than one thousand papers, and demonstrated the phase-selective synthesis of targeted zeolites from newly identified OSDAs. The computational approach allowed the synthesis of SSZ-39 (AEI) and SSZ-13 (CHA) zeolites under a wide range of conditions, relating broader synthetic accessibility windows to binding and geometric descriptors of templates. Furthermore, fine-tuning the charge distribution of OSDAs modulated the aluminum pairing in zeolites, as demonstrated for the CHA framework. Finally, the design toolkit also enabled us to synthesize an aluminosilicate CHA/AEI intergrowth from a single OSDA, showcasing opportunities for tuning catalytic properties by controlling zeolite phase competition. The integrated platform from this work is made available for the public (see the Data and materials availability statement) and is expected to markedly accelerate the design and optimization of zeolites.

[1]Department of Materials Science and Engineering, Massachusetts Institute of Technology, Cambridge, MA 02139, USA. [2]Department of Chemical Engineering, Massachusetts Institute of Technology, Cambridge, MA 02139, USA. [3]Instituto de Tecnología Química, Universitat Politècnica de València-Consejo Superior de Investigaciones Científicas, 46022 Valencia, Spain. [4]Department of Materials and Environmental Chemistry, Stockholm University, SE-106 91 Stockholm, Sweden.
*Corresponding author. Email: mmoliner@itq.upv.es (M.M.); rafagb@mit.edu (R.G.-B.)

Phase competition and literature data

To capture phase competition with atomistic simulations, we postulated that a selective OSDA must exhibit both strong binding affinity toward the desired host and weak binding affinity toward all other frameworks (*16*, *17*). To retroactively validate this hypothesis, we obtained 549 OSDAs from the literature using automated extraction tools (*18*, *19*). Then, we calculated the binding affinity of each OSDA toward 209 zeolite frameworks (fig. S1), generating a binding matrix (materials and methods and Fig. 1, A and B). More than 586,000 zeolite-OSDA poses across different frameworks, OSDAs, loadings, and initial conformations were generated using the computational pipeline shown in Fig. 1C (*20*, *21*). By selecting the pose that optimized the binding energy for each OSDA-zeolite pair, we obtained a binding matrix with ~112,400 entries. Phase selectivity was then quantified by comparing OSDAs and zeolites across the rows and columns of the binding matrix using two metrics: the directivity of an OSDA (D), or how close a molecule is to the best OSDA for a given framework, and the competitivity of a framework (C), or how close a zeolite is to the best host for the given OSDA (materials and methods and Fig. 1B). These quantities did not necessarily correlate with the conventional binding energies (fig. S2). As both the directivity and competitivity metrics were useful for optimizing zeolite-OSDA pairs, it was convenient to unify them under a single one-dimensional descriptor. We defined a quantity called templating energy (E_T) from the geometric mean of the Boltzmann average of each energy metric

$$E_T = -kT \log(C_{OSDA} D_{OSDA} C_{SiO2} D_{SiO2})^{1/4}$$

where T is a temperature, k is the Boltzmann constant, and C and D are the metrics of competition and directivity, respectively, normalized by either OSDA or SiO_2 (materials and methods). The templating energy quantifies the notion that a particular zeolite-OSDA pair is better over another if both the competition and directivity energies are favorable according to both normalizations (fig. S3).

The simulation data were then benchmarked on their ability to reproduce the 1122 zeolite-OSDA pairs extracted from the literature. We used the templating energy to rank the best OSDAs for a given zeolite and the best zeolites for a given OSDA. Because pairs not observed in the literature did not represent true negative data, only positive data points were used to assess the ranking scheme. Literature recall was quantified by plotting the cumulative number of positive OSDA-zeolite pairs recalled against the molecule/zeolite percentile (fig. S4). A perfect agreement between the binding metric and the literature data would lead to an area under the recall curve (AUC) equal to 1, and a random metric would have an AUC of 0.5. Figure 1D exemplifies the recall curve for some zeolites and OSDAs. For zeolites such as AEI or ZSM-5 (MFI), the AUC values were high, which suggests that the positive

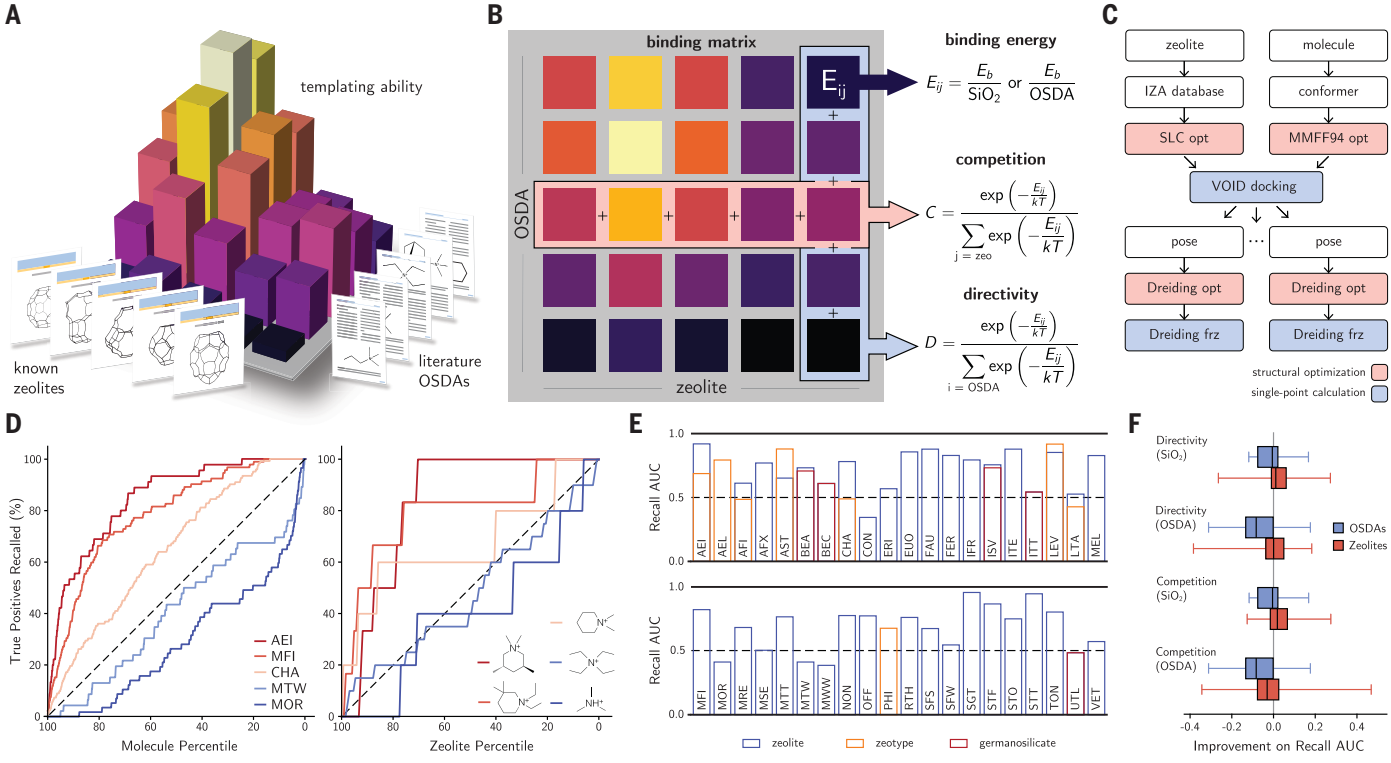

Fig. 1. Computational method used to quantify phase competition in zeolites. (**A**) OSDAs reported in the literature are docked into known zeolites, spanning a full matrix of binding energies. (**B**) Each element of the binding matrix is defined as the molecule-framework binding energy at the most favorable loading, normalized by the number of framework atoms or OSDA molecules (materials and methods). Along OSDAs, binding energies are ranked to determine how directive a molecule is toward a zeolite. Along zeolites, phase competition is quantified for a given OSDA. (**C**) Computational pipeline used to calculate binding energies for zeolite-OSDA pairs. (**D**) Explaining the literature with the templating energy. A recall curve is obtained by using the metric as a sorting algorithm for ranking OSDAs for a given zeolite (left) or zeolites for a given molecule (right). The dashed line indicates the expected recall curve for a random sorting algorithm. (**E**) Recall AUC for several zeolite frameworks according to their typical compositions. (**F**) Improvement of the recall AUC of OSDAs and zeolites using the proposed templating energy compared with other individual metrics. Including phase competition analysis improves the explanation of literature outcomes for ~70% of the zeolites in the literature.

pairs were systematically ranked high based on the templating energy metric. In fact, 34 of the 40 most common zeolite frameworks in the literature display AUC values higher than 0.5 (Fig. 1E), which demonstrates that the ranking scheme reproduced past synthesis outcomes. Only OSDAs for a few frameworks, such as ZSM-12 (MTW) and mordenite (MOR), were not accurately recalled by the ranking scheme. These hosts are often synthesized through OSDA-free routes or with small amines and thus are expected to appear as products in the presence of unselective OSDAs, with their synthesis dominated by factors beyond host-guest interactions, such as gel composition or temperature. Analogously to zeolites, the recall curves of OSDAs demonstrated that certain molecules were more selective than others. Smaller OSDAs typically have lower selectivity toward large cages and pores, and more complex, highly decorated OSDAs tend to be more selective (*22*). In keeping, zeotype structures have recall AUC on average 10% lower than that of their zeolite counterparts (Fig. 1E), as AlPO-type structures are frequently synthesized from smaller, less selective OSDAs (*22*). Additionally, a lower agreement between the literature and the binding metrics for certain frameworks suggested that binding energy metrics alone were limited predictors of synthesis outcomes in the context of Al-rich zeolites or dual-OSDA design. This is the case for zeolite A (LTA), for instance, which is typically synthesized using tetramethylammonium to selectively direct the formation of sod cages in combination with another OSDA to direct the formation of the lta cage (*23*), or CIT-1 (CON), whose intersecting pores allow OSDAs to create molecular aggregates that direct crystallization (*24*).

Finally, we demonstrated that the templating energy metric outperformed plain binding energies in recalling positive data points from the literature (Fig. 1F). When selecting molecules for a given zeolite, the templating energy explained the literature better for ~70% of the structures, for which the average improvement in AUC was 0.06 with respect to the binding energy per framework atom, which is the traditional metric of OSDA-zeolite affinity (fig. S5). On the other hand, the best hosts for a given OSDA were not well predicted by the templating energy, as the directivity component did not influence the structure-directing ability of an OSDA. Thus, we propose both a single aggregate parameter to design OSDAs that is effective for screening and independent energy metrics from which further insights could be derived.

OSDA design through phase competition and shape analysis

OSDAs must satisfy other design targets beyond binding energies. Physical descriptors of the OSDA molecular structure, for example, are useful predictors of templating ability and complement phase competition metrics (*25*). Often, the strongest host-guest interactions occur for well-defined OSDA volumes or shapes, but their interplay is not necessarily bijective. To describe the shape of OSDAs with low-dimensional parameters, we performed a principal components analysis (PCA) of the three-dimensional distribution of atomic coordinates of ground-state conformers into a

two-dimensional space (materials and methods and Fig. 2A). Additionally, we calculated the volume of each OSDA by using a voxel-based approach on the same conformers (materials and methods). The two PCA axes and the volume are useful parameters to describe the overall shape and size of a molecule and can be used as filters when proposing new OSDAs.

Designing molecules with targeted shapes, sizes, and selectivity can be performed in a purely computational manner, but other performance metrics of OSDAs, such as synthetic accessibility, are hard to evaluate algorithmically. By contrast, desiderata such as the intellectual novelty of molecules are more easily recognized by experts, whereas quantitative templating metrics are not. A human-computer partnership drastically accelerates the process of molecular design by combining chemical intuition with computationally selected leads (*26*, *27*). To navigate and visualize hundreds of thousands of zeolite-OSDA pairs and leverage shape similarity, chemical intuition, and domain expertise, we created an online database of zeolite-OSDA pairs containing all simulation outcomes of this work. This database, called Organic Structure-directing agent DataBase (OSDB), provides a graphical interface to query, select, and compare molecules as well as obtain information about prior art in the extracted literature and patents (fig. S6 and movie S1). Thus, all relevant design metrics were easily filtered and visualized in OSDB, allowing a computer-augmented design of OSDAs for targeted zeolites using interactive down-selection of candidates (movie S1). We illustrate this design process with several examples.

On the basis of the AUC analysis, our proposed metric showed high explanatory power for the small-pore zeolite AEI. The synthesis of the aluminosilicate SSZ-*39* with AEI framework is typically carried out using alkyl-substituted piperidinium cations as OSDAs, such as the computationally designed *N*-ethyl-*N*-methyl-2,2,6,6-tetramethylpiperidinium (OSDA **1**) (*28*), or the commercial *N*,*N*-diethyl-2,6-dimethylpiperidinium (OSDA **2**) (*29*) (Fig. 2B). According to our simulations, both OSDAs had favorable shapes for the AEI zeolite, with the nearly 1:1 aspect ratio at which binding affinities toward this framework were stronger (Fig. 2C). In fact, most OSDAs that are able to synthesize AEI with zeolite composition appeared at the top left region of the shape space, suggesting that shape and templating ability were correlated for this zeolite (Fig. 2C). Furthermore, OSDAs **1** and **2** exhibit excellent templating energy and volume to fill the aei cage (200 to 225 $Å^3$) (Fig. 2D). Nevertheless, their synthetic complexity, quantified by the SCScore proposed by Coley *et al.* (*30*), was higher than that of many other known or candidate OSDAs (Fig. 2E), suggesting higher preparation costs. In particular, the lower SCScore of OSDA **2** compared with OSDA **1** could be related to its usage as a commercial template for the industrial preparation of SSZ-*39*.

On the basis of the design strategies summarized by Fig. 2 and visualized in OSDB (movie S1), we proposed tris(dimethylamino)(methyl) phosphonium (OSDA ***3***) as a candidate for the synthesis of SSZ-*39*. It not only displayed favorable volume (Fig. 2D) and phase competition metrics (fig. S7) toward the AEI framework, but also showed considerably lower synthetic complexity than piperidinium-type cations (Fig. 2E). Following this lead, SSZ-*39* was first prepared using OSDA ***3*** under the following synthesis conditions: 1 SiO_2: 0.036 Al_2O_3: 0.3 OSDA ***3***: 0.2 NaOH: 15 H_2O, using the high-silica FAU CBV720 as the Si/Al source, and with the crystallization carried out at 135°C for 7 days. The main physicochemical characteristics of this material are summarized in fig. S8, showcasing tetrahedrally coordinated Al species in framework positions as well as crystalline nature and textural properties comparable to an AEI zeolite synthesized with baseline commercial OSDAs.

We evaluated the selectivity of computationally designed OSDA ***3*** by comparing its ability to crystallize AEI against a known, also phosphorous-containing template for this framework, tetraethylphosphonium (OSDA ***4***). Instead of using the high-silica FAU zeolite (Zeolyst, CBV720) as the Si and Al source, we used fumed silica as the Si source and the low-silica FAU (CBV500) as the Al source, thereby lowering the overall cost of the synthesis but increasing the difficulty in crystallizing the target zeolite. The synthesis of SSZ-*39* was attempted under the following conditions: 1 SiO_2: 0.091 or 0.125 Al_2O_3: 0.2 OSDA ***3*** or ***4***: 0.25 NaOH: 5 H_2O. Although OSDA ***4*** did not yield AEI in either of these conditions, OSDA ***3*** successfully crystallized SSZ-*39* in both (fig. S9), attesting to the higher selectivity of the latter toward AEI. Although both OSDAs display similar shapes, OSDA ***3*** is closer to the ideal OSDA **1** than OSDA ***4*** (Fig. 2B), exhibiting more favorable templating and competition energies by ~1 kJ/mol and 5 kJ/mol SiO_2, respectively. These values suggested that the proposed computational metrics were effective in capturing the subtleties of template

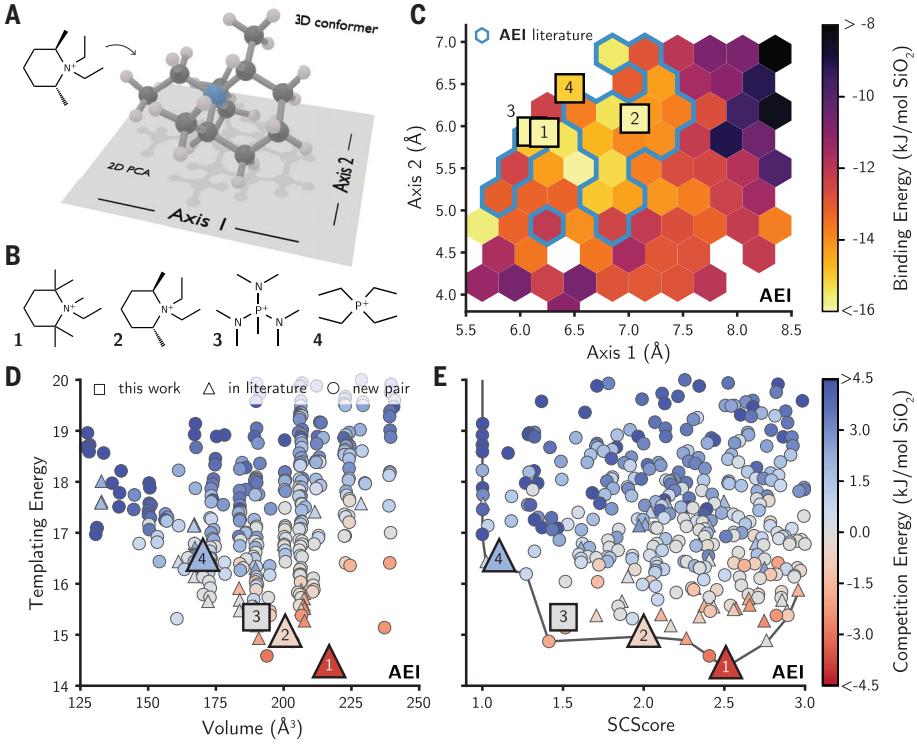

Fig. 2. OSDA selectivity for AEI zeolite. (**A**) Schematic on the shape representation of OSDAs. The three-dimensional conformation is converted into two axes by projecting the atomic coordinates into a two-dimensional space using PCA. (**B**) OSDA candidates for the synthesis of AEI. (**C**) Relationship between the shapes of OSDAs and their binding energies toward AEI. The color of each hexagon indicates the mean competition energy for all OSDAs within that area. Blue outlines indicate that at least one OSDA within that region is known to synthesize AEI with zeolite composition. (**D**) Templating energy of OSDAs against their volume. (**E**) Templating energy of OSDAs against their SCScore. The Pareto frontier is shown with a solid gray line.

selectivity during the OSDA design process despite the fine resolution of the zeolite-OSDA interaction energies. Our binding metrics were also effective at singling out highly selective OSDAs that led to the discovery of frameworks such as MFI, ITQ-4 (IFR), and ITQ-7 (ISV) (fig. S10). These results suggested that the proposed tools could not only identify new OSDAs for known structures, but that they hold potential to detect archetypical templates for unrealized zeolite topologies.

As a second example, we analyzed the interplay between OSDA shape and binding metrics in the experimental phase selectivity of CHA. Aluminosilicate CHA (SSZ-13) is typically synthesized using *N,N,N*-trimethyladamantammonium (TMAda, denoted here as OSDA **5**), a relatively expensive and complex OSDA (*31*) (Fig. 3A). Beyond TMAda, *N*-ethyl-*N,N*-dimethylcyclohexanaminium (OSDA **7**) has also been described for the synthesis of SSZ-13 as a simpler OSDA (*32*, *33*). Accordingly, our descriptors indicated that OSDAs **5** and **7** displayed similar shapes (Fig. 3B) and synthesis complexity (Fig. 3D), although OSDA **5** was closer to the ideal volume of 210 Å^3 than OSDA **7** (Fig. 3C).

To probe the influence of shape in the phase selectivity of zeolites, we compared the ability of OSDA **7** to synthesize CHA with that of *N,N,N*-trimethylcyclohexanaminium (OSDA **6**) (*34*) and *N,N*-diethyl-*N*-methylcyclohexanaminium (OSDA **8**) (*35*). OSDAs **6** to **8** had favorable binding and templating energies toward CHA (fig. S11) and were effective templates for this framework. Although they are chemically similar, their geometrical shapes were substantially different within the precision of our descriptors (Fig. 3B), and their binding strengths increased from OSDA **6** through **8**. A design approach considering only the binding metrics would predict OSDA **8** as the best template for CHA. To verify this hypothesis, we attempted the synthesis of SSZ-13 using these three templates under a variety of conditions, including using amorphous or high-silica crystalline Si and Al sources, different Si/Al and Na/Si ratios, and with and without the presence of seeds (fig. S12). As expected by its less favorable templating energy and poorer geometrical fit, OSDA **6** showed the narrowest synthesis windows among the three templates, being unable to fully crystallize CHA when high-silica FAU was used as a Si source under Na-free conditions (fig. S12A), or in most syntheses using amorphous sources (fig. S12, B and C). Notably, OSDA **7** outperformed OSDA **8** in more demanding synthesis conditions (fig. S12D), despite OSDA **7** having the weaker binding energy of the two. These results indicate that other effects may lower the experimental selectivity of OSDA **8** toward CHA compared with OSDA **7**. For example, the shape of OSDA **8** is further away from the ideal shape of OSDA **5** than OSDA **7**. When OSDA **8** was occluded in the chabazite cage, its shape experienced larger geometrical distortions to achieve the final, occluded conformation (fig. S13), which increased its free energy and reduced its ability to crystallize CHA. Thus, designing OSDAs with appropriate shapes and volumes may be as important as optimizing binding energies for improving phase selectivity in zeolite synthesis, particularly when molecules already exhibit favorable competition metrics toward the targeted frameworks.

Modulating aluminum distributions through OSDA design

Although dispersion interactions typically provide framework selectivity (*22*), electrostatic interactions between the framework and structure-directing agents rule heteroatom distributions, influencing the stability and catalytic properties of the product zeolite

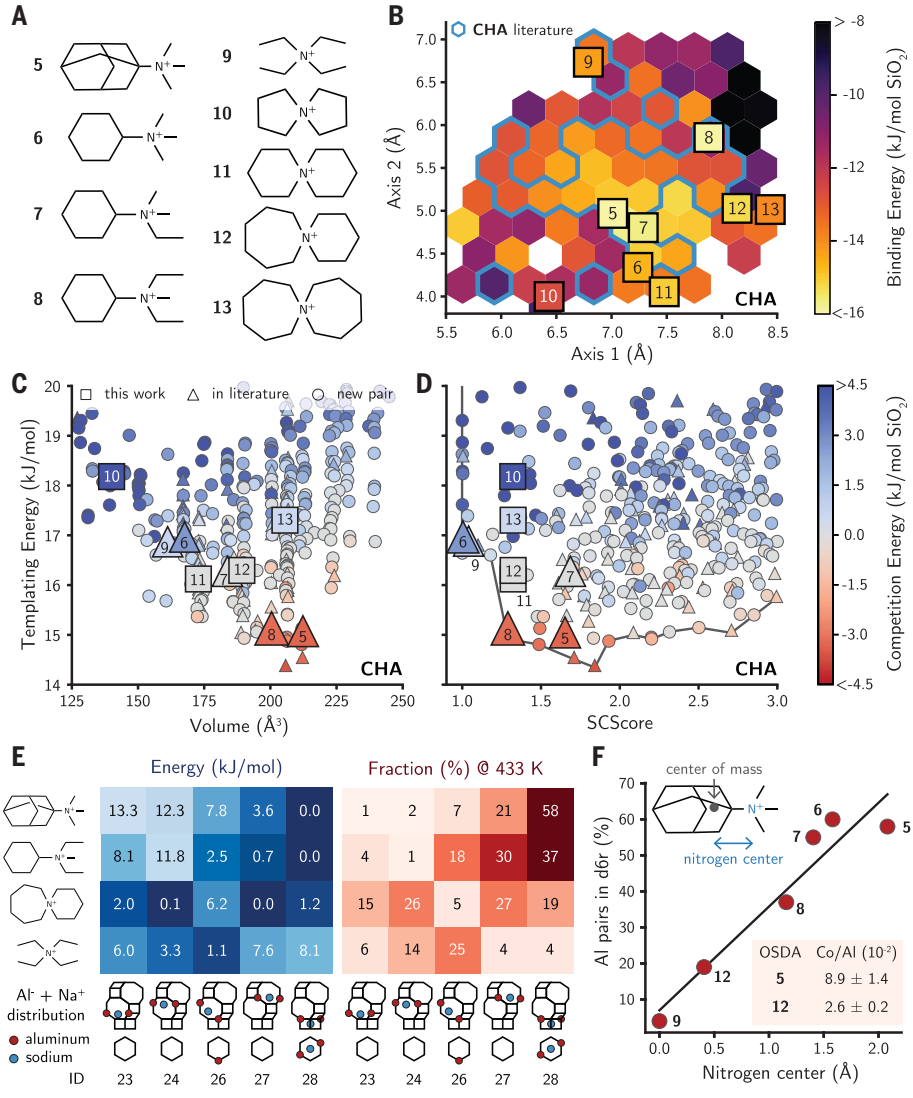

Fig. 3. OSDA selectivity for CHA zeolite. (**A**) OSDA candidates for the synthesis of CHA. (**B**) Relationship between the shapes of OSDAs and their binding energies toward CHA. The color of each hexagon indicates the mean competition energy for all OSDAs within that area. Blue outlines indicate that at least one OSDA within that region is known to synthesize CHA with zeolite composition. (**C**) Templating energy of OSDAs against their volume. (**D**) Templating energy of OSDAs against their SCScore. The Pareto frontier is shown with a solid gray line. (**E**) Influence of OSDA in the energy (blue) and fraction (red) of aluminum pairs in the cha cage in the presence of sodium. The predicted fraction of aluminum pairs is calculated at 433 K. (**F**) Relationship between the nitrogen center and the fraction of aluminum pairs in d6r units (distribution 28) for different OSDAs. Molecules with larger separation between the center of mass and the nitrogen center favor the pairing of aluminum atoms in the d6r units. The solid line is a linear regression of the data. (Inset) Co/Al ratio from cobalt titration experiments for CHA samples synthesized with OSDAs **5** and **12**.

(*36*–*38*). OSDAs with strong affinity and distinct charge distribution may overcome natural aluminum biases and crystallize desired frameworks with tailored aluminum distributions. To screen for charge distribution in OSDAs without using electronic structure calculations, we proposed a geometric descriptor by taking the distance between the quaternary nitrogen atom in a monocationic OSDA to the center of the mass of the molecule (fig. S14A). This descriptor allowed us to compare molecules with different charge distributions and templating abilities toward CHA (fig. S14C). Accordingly, the commercially available tetraethylammonium (OSDA **9**) and spiro-type molecules (OSDAs **10** to **13**) were molecules with good templating energy for the synthesis of SSZ-13 and have charge distributions that considerably differ from TMAda (Fig. 3A and fig. S14C). Although alkyl-substituted spiro-type OSDAs have been used for the synthesis of CHA before (*39*), alkyl groups increase the complexity of the organic synthesis, potentially adding purification and separation steps, decreasing the overall product yields, and increasing the costs. Furthermore, alkyl substituents result in uncontrolled diastereomeric mixtures, which can have a substantial influence on the zeolite nucleation and crystallization processes (*40*, *41*). On the other hand, nonsubstituted spiro-type molecules are more easily prepared, as reflected by their lower SCScores compared with that of OSDA **5** (Fig. 3D). In particular, the 6-azaspiro[5.6] dodecan-6-ium (OSDA **12**) had a near-ideal volume for CHA (Fig. 3C). Although its templating energy was higher than that of OSDA **5**, it was comparable to the commercial OSDA **7** and lay near the Pareto frontier between templating energy and SCScore for OSDAs in CHA (Fig. 3D). This fact implied that OSDA **12** offered one of the best trade-offs between templating ability and synthetic complexity among the candidates studied in this work in addition to its distinctive charge distribution. Furthermore, despite having been previously described as an OSDA unable to synthesize CHA in various conditions (*42*), our calculations showed that OSDA **12** had favorable competition metrics toward CHA (fig. S15).

On the basis of these predictions, the synthesis of CHA using OSDA **12** was first performed using the following synthesis gel composition: 1 SiO_2: 0.036 Al_2O_3: 0.2 OSDA **12**: 0.3 NaOH: 15 H_2O at 150°C for 12 days, where the high-silica FAU CBV720 was used as the Si/Al source. The main physicochemical characteristics of this material are summarized in fig. S16, where the tetrahedrally coordinated Al species in framework positions are demonstrated along with a crystalline nature and textural properties similar to the baseline CHA. With this successful proof of concept, we compared the effect of templating for the broader family of spiro-type OSDAs **10** to **13** using our binding metrics and a wider range of synthesis

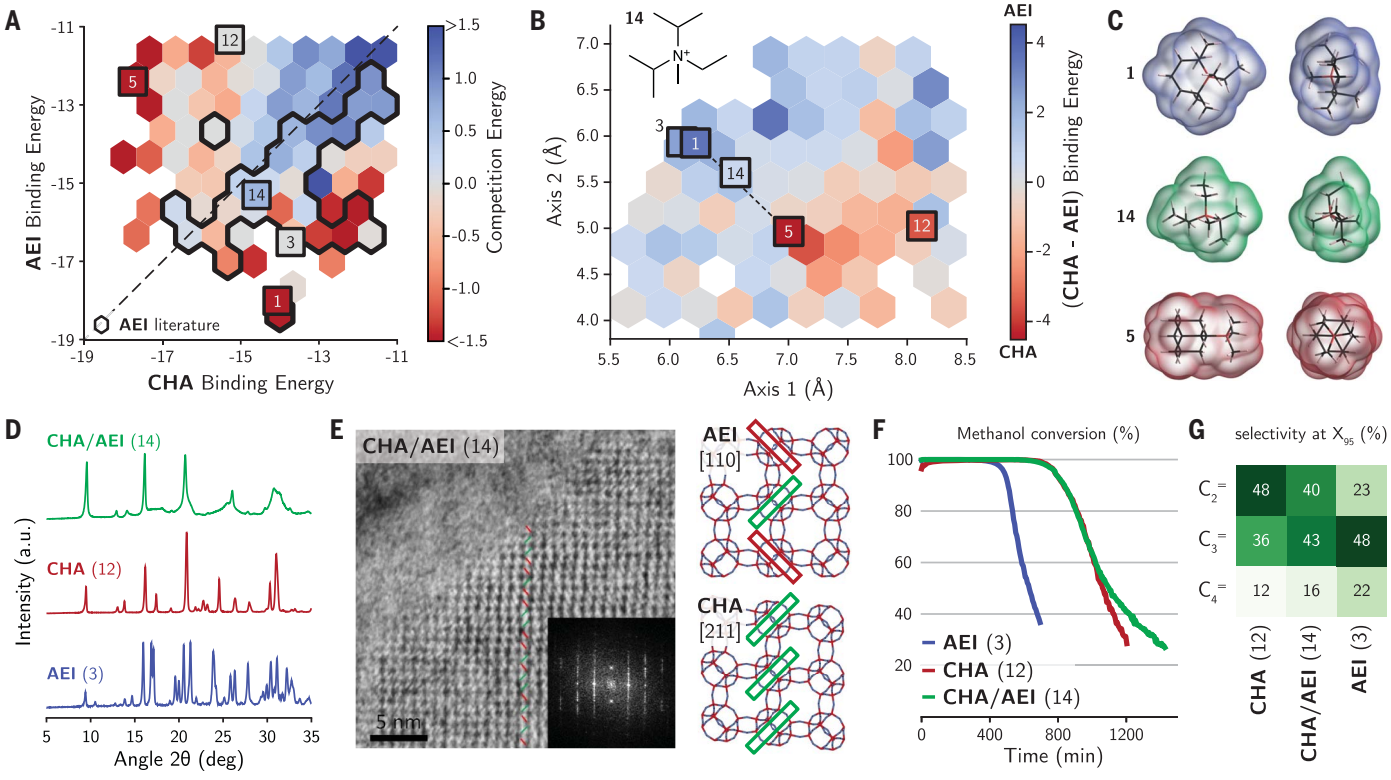

Fig. 4. CHA/AEI intergrowth zeolite. (**A**) Comparison between binding energies of OSDAs in CHA and AEI zeolites. The color of each hexagon indicates the mean competition energy for all OSDAs within that area. All energies are given in kilojoules per mole SiO_2. Black outlines indicate that at least one OSDA within that region is known to synthesize AEI with zeolite composition. (**B**) Relationship between the shapes of OSDAs and their binding energies toward CHA or AEI. Colors shifted toward red or blue indicate that the OSDA has a shape that favors the synthesis of CHA or AEI, respectively. OSDA **14**, the one that enables the CHA/AEI intergrowth, lies midway between the best OSDA for AEI (OSDA **1**) and the best OSDA for CHA (OSDA **5**). Energy difference is given in kilojoules per mole SiO_2. (**C**) DFT-calculated charge densities for OSDAs **1**, **5**, and **14**. OSDA **14** is between OSDAs **1** and **5** in terms of shape. (**D**) PXRD patterns of the as-prepared materials obtained with OSDAs **3** (AEI), **12** (CHA), and **14** (CHA/AEI). a.u., arbitrary units. (**E**) Integrated differential phase contrast–scanning transmission electron microscopy (iDPC-STEM) image of CHA/AEI as synthesized by OSDA **14** acquired from a sample sectioned using ultramicrotomy, and structural models for AEI and CHA showing the stacking patterns seen in the STEM image. (Inset) Fourier transform of the STEM image. (**F**) Comparison between methanol conversion profiles for CHA/AEI (OSDA **14**), CHA (OSDA **12**), and AEI (OSDA **3**). (**G**) Selectivity at X_{95} for CHA (OSDA **12**), AEI (OSDA **3**), and CHA/AEI (OSDA **14**). The selectivity of CHA/AEI (OSDA **14**) is between that of CHA (OSDA **12**) and AEI (OSDA **3**).

conditions. Figure S17A shows that OSDAs **10** and **13** were unable to crystallize CHA in the synthesis conditions tested, as predicted by their unfavorable shapes, volumes, templating energies, and phase selectivity toward CHA (Fig. 3, B and C, and fig. S15). On the other hand, OSDAs **11** and **12** displayed more favorable phase selectivity toward CHA and successfully crystallized the framework (fig. S17A). In particular, a better pore-filling effect from OSDA **12**, as evidenced by its larger volume, improved its selectivity toward SSZ-13 and exhibited a larger synthesis window, despite the comparable templating energies between OSDAs **11** and **12**. Additionally, OSDA **12** was able to crystallize CHA in more demanding conditions, such as using amorphous or Al-rich crystalline sources (fig. S17, D and E).

We then performed density functional theory (DFT) calculations, which explicitly account for electrostatics (*21*), to analyze the distribution of aluminum sites in the cha cage as a function of the OSDA (materials and methods). Because sodium is typically present in the reaction medium, it was included explicitly in the simulations as a cotemplate. By computing the relative energies of 48 different Al pairs for each molecule (*43*) (fig. S18), we found that different OSDAs imprinted different aluminum distribution onto the material (Fig. 3E and fig. S19). Assuming that the Al sites distributed themselves in the framework at the thermodynamic equilibrium of OSDA-zeolite interactions, energy differences could be translated into ensemble probabilities for the Al distribution at a given temperature (433 K in Fig. 3E and fig. S19). Although kinetic factors beyond OSDAs can also bias aluminum distributions, this equilibrium assumption struck a balance between accuracy and computational cost and enabled us to compare how OSDAs influenced aluminum pairing quantitatively and predictively. For the particular case of CHA, the equilibrium distribution of aluminum sites was found to be highly sensitive to the OSDA spatial charge distribution, and the nitrogen center descriptor showed a linear relationship with the fraction of aluminum pairs expected in d6r units (Fig. 3F). OSDAs with the nitrogen center closer to the center of the cha cage, such as OSDAs **9** or **12**, were less likely to form paired sites in the d6r units compared with the more polarized OSDAs **5** to **7**. Notably, OSDA **8** directed the formation of fewer paired aluminum sites in the d6r than OSDA **7** because of a larger distance between the nitrogen and the d6r unit imposed by the two ethyl groups. Although disentangling the effects of electrostatic and shape in the CHA (OSDA **8**) synthesis is not straightforward, the nearly equivalent charge distributions of OSDAs **5**, **6**, and **7** support the fact that the differences in phase selectivity between the three OSDAs were the result of templating effects rather than electrostatics.

Cotemplating of OSDA **12** and Na^+ was predicted to yield substantially fewer aluminum pairs in d6r units compared with cha cages synthesized with OSDA **5** and Na^+. To verify these predictions, we performed cobalt titration experiments to quantify Al pairing in CHA samples with similar physicochemical characteristics but synthesized with different OSDAs (materials and methods). Although cobalt titrations cannot fully characterize aluminum pairs because of uncertainties intrinsic to the technique, they are often useful for uncovering trends between samples (*44*). CHA crystals synthesized with OSDA **5** showed, on average, 3.4 ± 0.8 times as many Co^{2+} ions per aluminum than counterparts synthesized by OSDA **12** (Fig. 3F, inset, and fig. S20). This result was in quantitative agreement with the 3.05 ratio predicted by DFT and demonstrates that the newly proposed OSDA **12** provided a different aluminum bias when synthesizing CHA. As paired aluminum sites in the eight-membered ring of the cha cage are more relevant for catalytic applications (*38*), OSDA **12** may enhance the catalytic properties of CHA zeolites. Hence, controlling the distribution of aluminum sites through OSDA design may be a pathway to improve the performance of zeolite catalysts.

Finally, to analyze the cotemplating effect of sodium as the inorganic structure-directing agent, we used OSDA **12** with potassium hydroxide in the synthesis media. In these experiments, CHA was absent, and the EAB framework was detected instead (fig. S17E). Notably, OSDA **12** had the same binding energy toward the main cavities of both zeolites (−183 kJ/mol OSDA). We surmise that because the K^+ ion is too large to occupy the d6r position as directed by Na^+ (*43*), the gme cage of the EAB zeolite is favored instead. Therefore, the final zeolite crystallized by OSDA **12** had cages that solvated the template equally well, but the cooperation between inorganic and organic SDAs determined the other building units that crystallized the framework around the OSDA. This fact suggests that quantifying phase competition beyond zeolite-OSDA interactions could move the field beyond expert-informed selection of inorganic conditions and toward a fully automated prediction of zeolite synthesis.

OSDA design for intergrown zeolites

Intergrown zeolites offer distinctive properties compared with pure zeolite phases, such as different diffusional pathways and molecule confinements, or particular crystallographic environments to incorporate metallic active sites (*45*–*47*). Among the intergrown catalysts of industrial relevance, the silicoaluminophosphate (SAPO) form of CHA/AEI has shown distinct product selectivity and catalyst lifetime for the methanol-to-olefins (MTO) process compared with the pure crystalline CHA and AEI phases (*48*, *49*). However, SAPO-type catalysts have smaller hydrolytic and hydrothermal stability, as well as lower acidity compared with aluminosilicate zeolites. High-silica, intergrown small-pore zeolites (e.g., AFX/CHA) are often prepared using mixtures of OSDAs favorable for each individual zeolite (*50*, *51*). However, this dual OSDA approach requires empirically fine-tuning the synthesis parameters to avoid the crystallization of two independent zeolite phases, which substantially increases the complexity and cost of the process. To obtain a low-cost, aluminosilicate CHA/AEI intergrowth, we used our tools to design a single OSDA that crystallizes the targeted intergrown structure.

On the basis of the interplay between shape and binding shown in this work, we hypothesized that designing an OSDA for a targeted intergrowth required not only balancing phase competition, but also controlling the synthesis of structural motifs in the frameworks of interest (*52*). Figure 4A compares the binding energies of OSDAs toward AEI, CHA, and all other zeolites. Most of the OSDAs that synthesized AEI were more favorable toward this framework than toward CHA, as expected from our AUC analysis and traditional phase competition assumptions (*17*). The selectivity of OSDAs **1**, ***3***, **5**, and **12** to their product phases was also demonstrated by their distance from the equal-energy diagonal and low competition energy. Notably, the simulation outcomes revealed a phase boundary in the OSDA shape landscape (Fig. 4B). Stronger binders toward AEI fell within the region of OSDAs with aspect ratio closer to 1:1, and longer molecules favored the CHA framework. Differences of binding energies of OSDAs toward CHA and AEI highlighted these two distinct domains, shown in Fig. 4B with red and blue colors, respectively. From these two principles and after data exploration in OSDB (movie S1), we selected *N*-ethyl-*N*-isopropyl-*N*-methylpropan-2-aminum (OSDA **14**) as a potential candidate to direct the crystallization of the CHA/AEI intergrowth. OSDA **14** had comparable binding energies to both pure phases (fig. S21), and its shape lay on the phase boundary between the two frameworks. In fact, OSDA **14** resembled an interpolation between the best OSDAs for AEI (OSDA **1**) and CHA (OSDA **5**) both in the shape space (Fig. 4B) and when the OSDAs are visualized with their charge densities (Fig. 4C).

On the basis of this theoretical lead, a CHA/AEI intergrowth was prepared under synthesis conditions similar to the ones successfully used in the previous examples: 1 SiO_2: 0.036

Al_2O_3: 0.3 OSDA **14**: 0.2 NaOH: 15 H_2O, with the crystallization carried out at 140°C for 5 days. The powder x-ray diffraction (PXRD) pattern of the as-prepared material showed broadened peaks at angles mainly characteristic of CHA (Fig. 4D). Additional smeared peaks also appeared at angles compatible with the AEI phase, confirming the presence of both phases in the solid. To rule out the presence of a physical mixture of crystalline particles, the as-prepared sample was imaged by scanning electron microscopy, revealing uniform particles with an average size of ~200 nm (fig. S22A). OSDA **14** molecules remained intact after the hydrothermal synthesis of the CHA/AEI (OSDA **14**) sample (table S1 and fig. S22B). The PXRD pattern of the calcined form of CHA/AEI (OSDA **14**) indicated that the sample was formed by a 50:50 CHA:AEI intergrowth as compared with DIFFaX simulations (figs. S23 and S24). High-resolution scanning transmission electron microscopy images confirmed the intergrowth structure (Fig. 4E), showing an alternating stacking sequence caused by the orientation of the d6r units in CHA and AEI frameworks. The intergrowth CHA/AEI material showed a Si/Al molar ratio of 11 (table S2) and a micropore volume of ~0.28 cm^3/g, similar to those of the pure AEI and CHA materials.

To illustrate the application of the intergrowth, the structure was tested as a catalyst for the MTO reaction at 350°C (Fig. 4F). The X_{95} catalyst lifetime observed for the CHA/AEI (OSDA **14**) material was 788 min, which was similar to that of the CHA (OSDA **12**) catalyst reported in this work. We speculate that different active site distributions along cha and aei cavities influenced the overall diffusion pathways of the reaction-involved light olefins, thereby affecting the catalyst deactivation mechanisms. However, more fundamental characterization work should be done to elucidate this phenomenon. Regarding product selectivity, the CHA/AEI intergrowth showed the production of equivalent amounts of ethylene and propylene (~40 to 42%; table S3 and fig. S25) and ~16% of butene (table S3). These olefin selectivities were between the values achieved for the pure phases (Fig. 4G), as also shown by the $C_3^=/C_2^=$ and $C_4^=/C_2^=$ ratios (table S3), which further supports the claim that the product selectivity for the MTO reaction was governed by the zeolite cages present in the final intergrown crystals.

Conclusions

High-throughput computation allows for the control of phase competition in zeolite synthesis beyond Edisonian approaches that have dominated zeolite synthesis to date. Proposed metrics of phase competition, retroactively validated on comprehensive literature data, identified selective OSDAs through energetic, geometric, and electrostatic arguments. In three examples, competition was suppressed by designing OSDAs with favorable shapes, sizes, and binding metrics, achieving pure phases with wider synthesis windows. Reciprocally, it was possible to tailor intergrowths by designing a single OSDA that balanced phase competition both through shape and binding metrics. The ability of the method to recover literature outcomes from noncharged simulations suggested that product zeolites could often be predicted using only dispersion interactions. However, the final product is often dependent on cotemplating effects between inorganic and organic SDAs. Additionally, tuning OSDA charge and polarization modulates the aluminum distribution of the crystallized CHA zeolite, which can have important implications for catalysis. The computational results on templating effects can be further used to train data-driven selectivity models based on molecular structure descriptors, increasing the breadth of high-throughput screening undertakings. At the same time, developing more general electrostatic descriptors may also guide the investigation of aluminum distributions in zeolites beyond CHA. Finally, interactive visualization and analysis of said data through the OSDB portal is expected to empower domain experts to leverage these advances and accelerate the discovery cycle of zeolites.

REFERENCES AND NOTES

1. W. Vermeiren, J.-P. Gilson, *Top. Catal.* **52**, 1131–1161 (2009).
2. Y. Li, L. Li, J. Yu, *Chem* **3**, 928–949 (2017).
3. M. Moliner, F. Rey, A. Corma, *Angew. Chem. Int. Ed.* **52**, 13880–13889 (2013).
4. P. Eliášová *et al*., *Chem. Soc. Rev.* **44**, 7177–7206 (2015).
5. E. M. Gallego *et al*., *Science* **355**, 1051–1054 (2017).
6. D. W. Lewis, D. J. Willock, C. R. A. Catlow, J. M. Thomas, G. J. Hutchings, *Nature* **382**, 604–606 (1996).
7. G. Sastre, A. Cantin, M. J. Diaz-Cabañas, A. Corma, *Chem. Mater.* **17**, 545–552 (2005).
8. J. E. Schmidt, M. W. Deem, M. E. Davis, *Angew. Chem. Int. Ed.* **53**, 8372–8374 (2014).
9. F. Daeyaert, F. Ye, M. W. Deem, *Proc. Natl. Acad. Sci. U.S.A.* **116**, 3413–3418 (2019).
10. K. Muraoka, W. Chaikittisilp, T. Okubo, *Chem. Sci.* **11**, 8214–8223 (2020).
11. R. Pophale, F. Daeyaert, M. W. Deem, *J. Mater. Chem. A Mater. Energy Sustain.* **1**, 6750–6760 (2013).
12. K. Muraoka, Y. Sada, D. Miyazaki, W. Chaikittisilp, T. Okubo, *Nat. Commun.* **10**, 4459 (2019).
13. C. Baerlocher, L. B. McCusker, Database of Zeolite Structures (2021); www.iza-structure.org/databases/.
14. M. M. J. Treacy, I. Rivin, E. Balkovsky, K. H. Randall, M. D. Foster, *Microporous Mesoporous Mater.* **74**, 121–132 (2004).
15. M. W. Deem, R. Pophale, P. A. Cheeseman, D. J. Earl, *J. Phys. Chem. C* **113**, 21353–21360 (2009).
16. P. Wagner *et al*., *J. Am. Chem. Soc.* **122**, 263–273 (2000).
17. A. W. Burton, G. S. Lee, S. I. Zones, *Microporous Mesoporous Mater.* **90**, 129–144 (2006).
18. Z. Jensen *et al*., *ACS Cent. Sci.* **5**, 892–899 (2019).
19. Z. Jensen *et al*., *ACS Cent. Sci.* **7**, 858–867 (2021).
20. D. Schwalbe-Koda, R. Gomez-Bombarelli, *J. Phys. Chem. C* **125**, 3009–3017 (2021).
21. D. Schwalbe-Koda, R. Gómez-Bombarelli, *J. Chem. Phys.* **154**, 174109 (2021).
22. R. F. Lobo, S. I. Zones, M. E. Davis, *J. Incl. Phenom. Macrocycl. Chem.* **21**, 47–78 (1995).
23. A. Corma, F. Rey, J. Rius, M. J. Sabater, S. Valencia, *Nature* **431**, 287–290 (2004).
24. B. H. Toby, N. Khosrovani, C. B. Dartt, M. E. Davis, J. B. Parise, *Microporous Mesoporous Mater.* **39**, 77–89 (2000).
25. R. E. Boyett, A. P. Stevens, M. G. Ford, P. A. Cox, *Zeolites* **17**, 508–512 (1996).
26. R. Gómez-Bombarelli *et al*., *Nat. Mater.* **15**, 1120–1127 (2016).
27. M. Moliner, Y. Román-Leshkov, A. Corma, *Acc. Chem. Res.* **52**, 2971–2980 (2019).
28. J. E. Schmidt, M. W. Deem, C. Lew, T. M. Davis, *Top. Catal.* **58**, 410–415 (2015).
29. S. I. Zones, Y. Nakagawa, S. T. Evans, G. S. Lee, Zeolite SSZ-39, US Patent 5,958,370 (1999).
30. C. W. Coley, L. Rogers, W. H. Green, K. F. Jensen, *J. Chem. Inf. Model.* **58**, 252–261 (2018).
31. S. I. Zones, *J. Chem. Soc., Faraday Trans.* **87**, 3709–3716 (1991).
32. G. Cao, M. M. Mertens, A. S. Guram, H. Li, J. C. Yoder, Synthesis of chabazite-containing molecular sieves and their use in the conversion of oxygenates to olefins, US Patent 7,754,187 (2007).
33. X. Wang *et al*., *Chem. Commun.* **51**, 16920–16923 (2015).
34. T. M. Davis, S. Elomari, S. I. Zones, Method for preparing cha-type molecular sieves using colloidal aluminosilicate, US Patent 2014/0147378 (2014).
35. G. Cao, M. Mertens, A. S. Guram, H. Li, J. C. Yoder, Synthesis of chabazite-containing molecular sieves and their use in the conversion of oxygenates to olefins, US Patent 2008/0045767 (2008).
36. J. R. Di Iorio, C. T. Nimlos, R. Gounder, *ACS Catal.* **7**, 6663–6674 (2017).
37. E. M. Gallego *et al*., *Chemistry* **24**, 14631–14635 (2018).
38. F. Göltl, S. Bhandari, M. Mavrikakis, *ACS Catal.* **11**, 7719–7734 (2021).
39. Y. Nakagawa, G. S. Lee, T. V. Harris, L. T. Yuen, S. I. Zones, *Microporous Mesoporous Mater.* **22**, 69–85 (1998).
40. M. Dusselier *et al*., *Chem. Mater.* **27**, 2695–2702 (2015).
41. C. Kim, S.-J. Hwang, A. W. Burton, S. I. Zones, *Microporous Mesoporous Mater.* **116**, 227–232 (2008).
42. R. Millini, L. Carluccio, F. Frigerio, W. O'Neil Parker Jr., G. Bellussi, *Microporous Mesoporous Mater.* **24**, 199–211 (1998).
43. J. R. Di Iorio *et al*., *J. Am. Chem. Soc.* **142**, 4807–4819 (2020).
44. J. R. Di Iorio, R. Gounder, *Chem. Mater.* **28**, 2236–2247 (2016).
45. H. Kosslick *et al*., *J. Chem. Soc., Faraday Trans.* **90**, 2837–2844 (1994).
46. T. Willhammar *et al*., *Nat. Chem.* **4**, 188–194 (2012).
47. J. S. Bates, B. C. Bukowski, J. W. Harris, J. Greeley, R. Gounder, *ACS Catal.* **9**, 6146–6168 (2019).
48. L. Guo *et al*., *Ind. Eng. Chem. Res.* **57**, 10398–10402 (2018).
49. R. L. Smith *et al*., *Appl. Catal. A Gen.* **505**, 1–7 (2015).
50. Y. Naraki, K. Ariga, K. Nakamura, K. Okushita, T. Sano, *Microporous Mesoporous Mater.* **254**, 160–169 (2017).
51. G. Cao *et al*., Chabazite-containing molecular sieve, its synthesis and its use in the conversion of oxygenates to olefins, US Patent 7,094,389 B2 (2006).
52. D. Schwalbe-Koda, Z. Jensen, E. Olivetti, R. Gómez-Bombarelli, *Nat. Mater.* **18**, 1177–1181 (2019).
53. J. Towns *et al*., *Comput. Sci. Eng.* **16**, 62–74 (2014).
54. D. Schwalbe-Koda, learningmatter-mit/VOID: VOID 1.0.1., version 1.0.1, Zenodo (2021); https://doi.org/10.5281/zenodo.5260054.
55. D. Schwalbe-Koda, learningmatter-mit/gulpy: GULPy 1.0., version 1.0, Zenodo (2021); https://doi.org/10.5281/zenodo.5260056.
56. B. Blaiszik *et al*., *JOM* **68**, 2045–2052 (2016).
57. B. Blaiszik *et al*., *MRS Commun.* **9**, 1125–1133 (2019).
58. D. Schwalbe-Koda, R. Gómez-Bombarelli, Data for: Ab initio control of zeolite synthesis and intergrowth with high-throughput simulations, Data set, Materials Data Facility (2021); https://doi.org/10.18126/C5Z9-ZEJ7.
59. D. Schwalbe-Koda, learningmatter-mit/Zeolite-Phase-Competition: Article data for: Ab initio control of zeolite

phase competition and intergrowth with high-throughput simulations, version 1.0, Zenodo (2021); https://doi.org/10.5281/zenodo.5272354.

ACKNOWLEDGMENTS

The Electron Microscopy Service of the UPV is acknowledged for their help in sample characterization. J. Martínez-Triguero and C. Li are also acknowledged for helpful discussions on the MTO reaction, and B. Blaiszik is acknowledged for help with persistent data storage at the Materials Data Facility. **Funding:** D.S.-K. and R.G.-B. acknowledge the Energy Initiative (MITEI) and MIT International Science and Technology Initiatives (MISTI) Seed Funds. D.S.-K. was also funded by the MIT Energy Fellowship. C.P., E.B.-J., M.M., and A.C. acknowledge financial support by the Spanish government through the "Severo Ochoa" program (SEV-2016-0683, MINECO) and grant RTI2018-101033-B-I00 (MCIU/AEI/FEDER, UE). E.B.-J. acknowledges the Spanish government for an FPI scholarship (PRE2019-088360). Z.J., E.O., S.K., and Y.R.-L. acknowledge partial funding from Designing Materials to Revolutionize and Engineer our Future (DMREF) from the National Science Foundation (NSF); awards 1922311, 1922372, and 1922090; and the Office of Naval Research (ONR) under contract N00014-20-1-2280. S.K. was additionally funded by the Kwanjeong Educational Fellowship. Z.J. was also supported by the Department of Defense (DoD) through the National Defense Science Engineering Graduate (NDSEG) fellowship program. T.W. acknowledges financial support by the Swedish Research Council (grant no. 2019-05465). Computer calculations were executed at the Massachusetts Green High-Performance Computing Center with support from MIT Research Computing and at the Extreme Science and Engineering Discovery Environment (XSEDE) (*53*) Expanse through allocation TG-DMR200068. **Author contributions:** D.S.-K. designed and executed the simulations, computational analysis, and software development. C.P. carried out the design and synthesis of the OSDAs. S.K. and E.B.-J. performed the synthesis and characterization of zeolites. E.B.-J. executed the MTO experiments. T.W. performed the transmission electron microscopy analysis of the CHA/AEI intergrowth and the simulation of the PXRD patterns of different CHA/AEI intergrown phases. Z.J. and E.O. provided the literature data. R.G.-B. conceived the project and supervised the computational research. M.M., Y.R.-L., and A.C. supervised the experimental research. D.S.-K., M.M., and R.G.-B. wrote the first manuscript draft. All authors contributed to the analysis of the data and to the final manuscript. **Competing interests:** The authors are coinventors on two patent applications based on the materials synthesized in this work. **Data and materials availability:** The code used to automate the simulations of this work is available at Zenodo (*54*, *55*). Literature data are available in (*19*). Results of atomistic simulations are available at the Materials Data Facility (*56*, *57*) through the accession code available at (*58*). An interface to these data is available online at OSDB (http://zeodb.mit.edu/). The code and data used to produce all graphs in the manuscript are available at Zenodo (*59*). All other data needed to evaluate the conclusions of the paper are present in the paper or the supplementary materials.

SUPPLEMENTARY MATERIALS

science.org/doi/10.1126/science.abh3350
Materials and Methods
Figs. S1 to S25
Tables S1 to S3
References (*60*–*80*)
Movie S1

5 March 2021; resubmitted 14 July 2021
Accepted 31 August 2021
Published online 16 September 2021
10.1126/science.abh3350

Science

A priori control of zeolite phase competition and intergrowth with high-throughput simulations

Daniel Schwalbe-KodaSoonhyoung KwonCecilia ParisEstefania Bello-JuradoZach JensenElsa OlivettiTom WillhammarAvelino CormaYuriy Román-LeshkovManuel MolinerRafael Gómez-Bombarelli

Science, 374 (6565), • DOI: 10.1126/science.abh3350

Selectivity control in zeolite synthesis

Zeolites are widely used in many industrial applications, but despite decades of research, their synthesis still relies on trial-and-error approaches. Complex nucleation mechanisms and topological diversity lead to strong phase competition, complicating the issue of rational design of zeolite synthesis. Using atomistic simulations, literature mining, human-computer interaction, synthesis, and characterization, Schwalbe-Koda *et al*. developed a computational strategy that enables a priori control of phase selectivity in zeolite synthesis (see the Perspective by Chaikittisilp and Okubo). This approach uses several metrics for designing organic structure–directing agents to crystallize target zeolites with controlled phase competition and intergrowth. These results may have profound implications for the materials science community if this method is shown to be successful in the synthesis of practically useful uncommon zeolites. —YS

Science (ISSN) is published by the American Association for the Advancement of Science. 1200 New York Avenue NW, Washington, DC 20005. The title *Science* is a registered trademark of AAAS.